CHALMERS

Research Report 2005:5
ISSN 1652:8549

The Near Field Acoustics of a Generic Side Mirror based on an Incompressible Approach

Jonas Ask[†‡] and Lars Davidson[†]

[†] Division of Fluid Dynamics
Department of Applied Mechanics
CHALMERS UNIVERSITY OF TECHNOLOGY

[‡] Fluid Dynamic Center
VOLVO CAR CORPORATION
Göteborg, Sweden

1 Introduction

Flow induced noise experienced by the driver or passengers of a ground vehicle can be a consequence of different flow or fluid-structure phenomena occurring in low Mach number flows. Exposed components such as side mirrors, A-posts, rails, tires and underfloor details generate flow structures, which are the primary sources of noise generation around the vehicle above approximately 120 km/h. The present work studies the flow past a generic side mirror mounted on flat plate with respect to sound generation and propagation. This geometry has been the subject of several studies [1–5]. Höld and Siegert [1, 2] conducted both experimental and numerical investigations to predict sound generation and propagation at the Reynolds number of $Re_D = 7.066 \cdot 10^5$ based on the mirror diameter. They conducted URANS simulations for three different mesh densities and used a classic acoustic analogy to compute the radiated sound based on the surface pressure and its temporal derivative [6, 7]. The simulation time in their work covered 0.1 seconds. A similar study at the Reynolds number of $Re_D = 5.2 \cdot 10^5$ was reported in Rung et al. [3] which focused on differences in sound generation and propagation in comparisons of URANS and the Detached Eddy Simulation (DES) modeling technique. The maximum simulation time in their study covered 0.26 seconds, and the grid density was twice the highest resolved case in Siegert et al. [1, 2]. Results of Rung's DES simulation generally showed an overprediction of the low frequency fluctuating pressure levels for most surface mounted sensors and microphones. Their findings showed however a major improvement in acoustic results using the DES model as compared with the URANS results. The code vendor EXA later used the generic side mirror to validate their CAA method development in an aero acoustic consortium directed toward car manufacturers worldwide. They used the same Reynolds number as Rung et al. but avoided the difficulties associated with detailed separation control by introducing a "trip wire" in the simulations that was not present in the experiments. Their simulation covered 0.67 seconds and showed the same trends as reported in Rung et al. but had improved high frequency contents. Another code vendor, FLUENT, followed the experiment reported in [1, 2] at the higher Reynolds number. Their prediction of the radiated sound past the mirror was promising,

but confusing figures raise the question of where the monitoring points were actually located.

The present paper is a first attempt to investigate the flow and acoustics of the generic side mirror at the Reynolds number of $Re_D = 5.2 \cdot 10^5$ with a focus on the upstream laminar separation. This work uses the DES model. Several authors have previously reported promising results for similar geometries and flow fields with this technique [8–13]. In contrast to previous simulations conducted over the generic side mirror, a "trip-less" approach is chosen to capture an eventual laminar separation. This methodology was pioneered by Shur et al. [14] and has been further investigated in [8, 9, 13, 15] for cylinders and spheres. Shur and Spalart [14] used this methodology for URANS simulations in two dimensions past a circular cylinder, and three-dimensional investigations were conducted by Travin, Strelets and Constantinescu et al. [8, 9, 13]. The basic idea is that a laminar separation combined with a turbulent simulation strategy requires a sufficiently low upstream production of turbulent viscosity to be successful while maintaining the turbulence levels in the downstream wake and boundary layers. A description of the approach is presented in Section 2 below.

The most straightforward way to compute the near field acoustics of a flow is to conduct a compressible DNS. With this approach it is possible to directly evaluate sound emissions at any position in the computational domain. If interest is instead in finding the emissions at points outside the computational domain or from an incompressible flow field, a different strategy must be used. For flows where walls are present, a feasible method is to use either Ffowkes-Williams and Hawkings or Lighthill-Curle's analogy [6, 16]. These analogies convert the governing momentum and continuity equations to an inhomogeneous wave equation and are identical for steady and impermeable integration surfaces. Two major assumptions are made in these analogies:

- The fluctuating density, which is the dependent variable, exist on both sides of the equation and thus decouples the sound wave operator from the sources. This is a reasonable assumption for low Mach number flows, where sound emissions are primarily caused by the hydrodynamics.

- Only isotropic wave propagation is taken into account, which is

true only for flows with zero mean motion.

Studies of the incompressible assumption combined with a modified version of Lighthill-Curle's analogy were presented in Ask and Davidson [17,18]. The incompressible assumption is controversial and strictly speaking not valid for any flow field, but the results were promising in terms of both directivity and sound pressure levels. The modified version of Lighthill-Curle's analogy, Eq. 1, uses the temporal derivatives inside the integral instead of keeping the spatial derivatives outside the integral, as Curle's [16] original formulation states.

$$
\begin{aligned}
&p(\mathbf{x},t) - p_\infty = \\
&\frac{1}{4\pi}\int\limits_V \left[\frac{l_i l_j}{a_\infty^2 r}\ddot{T}_{ij} + \frac{3l_i l_j - \delta_{ij}}{a_\infty r^2}\dot{T}_{ij} + \frac{3l_i l_j - \delta_{ij}}{r^3}T_{ij}\right] dV(\mathbf{y}) \\
&+\frac{1}{4\pi}\int\limits_S l_i n_j \left[\frac{\dot{p}\delta_{ij} - \dot{\tau}_{ij}}{a_\infty r} + \frac{p\delta_{ij} - \tau_{ij}}{r^2}\right] dS(\mathbf{y})
\end{aligned}
\tag{1}
$$

In Eq. 1 the acoustic pressure fluctuations at an observer located at $\mathbf{x}$ are evaluated from a forward time projection of two integrals evaluated at the source location, $\mathbf{y}$. The first integral contains the volume contribution where $T_{ij} = \rho u_i u_j - \tau_{ij} + (p - a_\infty^2\rho)\delta_{ij}$ is commonly referred to as the Lighthill tensor. The dot(s) above T_{ij}, τ_{ij} and p denote time derivative(s), and l_j is the unit vector pointing from the source to the observer; the terms in this integral are often referred to as quadrapole terms. The second integral contains the surface integral and consists mainly of the fluctuating pressure and the fluctuating pressure temporal derivative. These terms are commonly referred to as dipole terms and are often regarded as the dominating terms for low Mach number flows. The derivation of the expression above can be found in [19] and the corresponding version of Ffowkes-Williams and Hawkings equation can be found in Brentner and Farassat [7] for the conditions mentioned above. A similar version is also implemented in the current version of FLUENT and is used in the present paper.

The methodology for evaluating the radiated sound involves two steps. First, the flow field is computed on the basis of the assumption of incompressibility and the DES modeling technique. From the flow field obtained, the fluctuating wall pressures are extracted and used in a second step to compute the radiated sound [6, 7, 17–19]. In this work the

volume sources are neglected owing to the storage cost. This means that the fluctuating wall pressure and the time derivative of the fluctuating wall pressure are the only terms treated.

The present paper is organized as follows. Section 2 discusses the flow state with respect to experiments and previous DES simulations conducted for both the geometry in question as well as similar objects. This is followed by a short review of different wall modeling techniques for LES (Section 3) and a description of the numerical approach used in the present simulation (Section 4). The result sections consist of the flow field results (Section 5) and the acoustic results (Section 6). Conclusions are presented in Section 7 and acknowledgments are stated in Section 8. Two appendixes are also included, first containing aspects of signal processing for truncated sequences (Appendix A) and the second giving the locations of pressure sensors and microphones (Appendix B).

2 Previous experimental and numerical investigations

The generic side mirror is geometrically similar to both the sphere and the cylinder, perhaps best known for their drag crisis around a critical Reynolds number. This great difference in drag force is the consequence of laminar versus turbulent separation over the object. The Reynolds number for the present simulation is $Re_D = 5.2 \cdot 10^5$, which is close to the critical Reynolds number for both the sphere and the cylinder. According to Schlichting [20], the drag force coefficient over a circular cylinder drops 0.7 over the interval $3.0 \cdot 10^5 < Re_D < 5.0 \cdot 10^5$. Similar results can also be found for the sphere, where the force coefficient drops 0.31 over the interval $2.5 \cdot 10^5 < Re_D < 4 \cdot 10^5$. Constantinescu and Squires [12] mention a critical Reynolds of $Re_{cr} \approx 3.7 \cdot 10^5$ for the sphere, which agrees well with Schlichting [20]. If an analogy is made between the flow state over the side mirror and the corresponding sphere and cylinder, the boundary layer over the generic side mirror in the present state is close to its critical value. An issue that emphasizes this problem is two different experimental results for the same flow conditions. The first is the work presented by Rung et al. [3], who state:

> ”Oil-flow visualization revealed that flow is clearly super-

> critical, with transition occurring approximately $0.15D$ upstream of rear-face edge."

Secondly, personal communication with Daimler-Chrysler [21] and information obtained through FORD [4] showed that subsequent measurements indicate, in contradiction with the anotation above, that the flow state over the mirror is actually sub-critical. In the EXA validation update report [4] the laminar separation point was found from oil-flow visualizations to occur approximately $0.13D$ upstream of the rear face of the mirror. This corresponds to $\alpha_{sep} \approx 75°$, measured from the most upstream point of the top-mounted quarter sphere.

According to Schlichting [20] the separation point of sub-critical flows past the sphere occurs at approximately $90°$, measured from the upstream stagnation point. The corresponding separation point of super-critical flows is at approximately $110°$. Flow simulations past a sphere were also conducted in Constantinescu and Squires [12] and showed separation points between $84°$ and $87°$ at the Reynolds number of $Re_D = 1 \cdot 10^4$. In another publication by the same author [13] the reported separation points for the sub-critical regime were $81.5°$ at $Re_D = 1 \cdot 10^5$ and between $103°$ and $120°$ for the super-critical regime.

The separation point of the sub-critical flow past a circular cylinder is stated in the literature to be expected to occur at approximately $80°$. In the simulations made by Travin et al. [8] the computed separation point for the sub-critical flow past a circular cylinder occurred at $78°$ to $95°$. The super-critical separation points in the same paper occurred at $93°$ to $111°$. The following conclusions can be drawn from the findings presented above:

- The separation point of sub-critical flows can be expected to occur farther upstream than is the case in super-critical flows
- The information on the separation point for the mirror in [4, 21] corresponds well with the corresponding location in the sub-critical flow past the cylinder

On the basis of this information it was further assumed that the flow state over the mirror is actually sub-critical, with an upstream laminar separation. The aim of the present simulation is thus to attempt to detect this laminar separation and study its effect on both sound generation and propagation.

As regards spatial discretization of the convective fluxes for DES, a general recommendation was made by Strelets [9] and further applied in [12, 13, 22, 23]. He suggested central difference schemes in the wake combined with high-order, upwind-biased schemes in the RANS and Euler regions if the pure central differenced scheme proved unstable. The central schemes are known to have stability issues when operating in RANS mode, especially for cells with large aspect ratios. On the other hand, upwind-biased schemes are commonly considered too dissipative for LES. Different spatial discretization practices have been used in connection with DES. In most extreme cases, a fifth-order, upwind-biased scheme was applied in the Euler and RANS region combined with a fourth-order central scheme in the wake [22, 23]. In [12, 13], a fifth-order upwind scheme was used close to the walls and over the Euler region and was combined with a second-order central difference scheme in the wake region. However, several authors have reported acceptable results also for second and third-order, upwind-biased schemes [3, 11] involving separated flows.

For smooth objects, where separation occurs, both wake characteristics and force coefficients are crucial to whether the separation occurs at laminar or turbulent flow states. There are several possible ways of treating these flow states. Three alternatives are presented here.

- The most common technique is to apply an inflow turbulence level. This technique will for some models cause an overprediction in turbulent quantities in stagnation regions.

- The second technique involves low inflow turbulence levels as well as a trip location known in advance or predicted by some other method. The trip location can either be a geometrical fix or reconstructed through source terms in the governing equations, Constantinescu and Squires [12].

- The third alternative will be further referred to in the following text as the ”trip-less” approach and was introduced by Shur et al. [14] for sub-critical flows past cylinders. This technique has thus far been used for two and three-dimensional flows over objects such as cylinders and spheres [8–10, 13] and involves the following steps. An initial RANS simulation is carried out. After this initialization, the inlet boundary condition is shifted to a zero or close to

a zero turbulent level while maintaining the freestream velocity level. The initial turbulence will then be swept out of the boundary layers on the upstream side of the geometry but will survive in the wake. The key to success in this method is the occurrence of separation, which is inevitable for objects such as cylinders and spheres.

3 Wall modeling techniques for high Reynolds number flows

In recent years LES has gained increased attention due to several successful applications. The key to this success has been moderate Reynolds numbers or approximations in typically one spatial direction. For high Reynold number flows past three-dimensional objects, wall resolved LES is still out of reach for most engineering applications. The primary cause of this limitation is the need to resolve the streaks typically present in the near-wall region. Many estimations of the required number of grid points to resolve these kinds of flow structures are found in the literature [3, 15, 24–26]. Chapman [24] estimated the grid requirement for resolving the viscous sublayer as

$$N_{xyz} \propto Re_L^{1.8} \tag{2}$$

for nested grids and flat plate boundary layers. This estimate is not far from the resolution requirements in DNS, where $N_{xyz} \propto Re_L^{2.25}$. Furthermore, Temmerman et al. [25] mention a grid dependency remote from walls as $N_{xyz} \propto Re^{0.4}$ in the outer region. This means that the outer region will typically contain only a fraction of the total number of grid points. In a more local perspective, these estimates can be expressed in terms of wall units for the first off-wall cells. In the wall normal direction the resolution in wall units is similar to the requirement for a low Reynolds model, with $n^+ \approx 1$. The limitation in a wall-resolved LES compared to RANS occurs in the streamwise (s^+) and spanwise (l^+) direction of the flow. Spalart [15] recommended for wall resolved LES that $s^+ \approx 50$; the corresponding recommendation in Davidson and Dahlström [27] was $s^+ \approx 100$. Davidson and Dahlström recommended $l^+ \approx 20$ in the streamwise direction, and similar values were presented

in Temmerman et al. [25]. To circumvent this bottleneck in computational requirement for wall-resolved LES, a wide range of techniques have been developed to reduce the computational effort necessary in the near-wall region. For this purpose a schematic overview of the different methods is presented in Fig. 1.

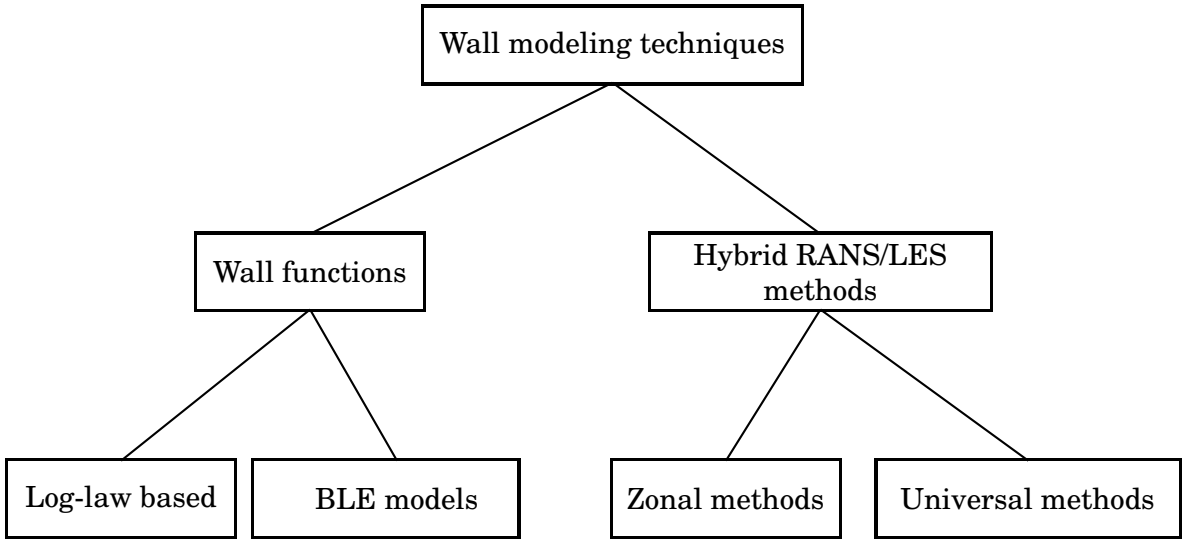

Figure 1: Overview of techniques for high wall bounded high Reynold number flows

One way to circumvent the near-wall resolution issues in LES is the use of wall functions. These functions replace the resolution requirement of the governing equations with an expression or value for the wall shear stress. Typical for these techniques is that the first off-wall cells are located in the logarithmic region $30 < n^+ < 300$ where the lower limit is most desirable. In its simplest form, log-law based wall functions assume logarithmic or semi-logarithmic velocity profiles that provide the wall shear stress as a boundary condition to the governing filtered or averaged equations and further assume that the turbulence is in a state of local equilibrium. The drawbacks in this assumption are well known for flows involving separation, stagnation and reattachment, where the wall shear stress vanishes. To increase the validity of

the wall functions, improvements have been made to include the pressure gradient [28] as well as replacing the wall shear stress in the velocity log-law with the turbulent kinetic energy [29]. However, these treatments still rely on an assumed logarithmic or semi-logarithmic velocity distribution, which drastically limits their validity.

Balaras and Benocci [30] presented a different approach to wall modeling that was based on filtered Navier-Stokes equations and used what appeared to be a high Reynolds grid. The filtered equations were solved down to the first grid point on this primary high Reynolds grid. From the first grid point and down to the wall, a refined mesh was embedded in the main mesh, where simpler two-dimensional boundary layer equations (BLE) were solved. The boundary layer equations give velocity profiles for the streamwise and spanwise components and thus provide the wall shear stress in order to be able to solve the outer filtered equations. The advantages of this technique are twofold. First, less empiricism is needed to compute the wall shear stress compared to the logarithmic based wall functions mentioned above. Secondly and most attractive is that the cumbersome procedure of building low Reynolds meshes are avoided. This is a major advantage in industrial applications where low Reynolds grids may prove almost impossible to generate due to the geometrical complexity. This technique was used in Cabot and Moin [31] for a backward facing step and was compared with wall resolved LES and showed promising results for both wall friction and wall pressure. However, as pointed out in Nicoud et al. [26], a strong dependency of local Reynolds number and the location of the first off-wall cell is vital for an accurate prediction of the velocity profiles, which can be problematic in separated flows. The technique was further investigated In Wang and Moin [32] for the airfoil trailing edge flow. The results showed a clear overprediction of the mean friction coefficient, which was argued to be caused by too high a turbulent viscosity. They suggested that a dynamically adjusted mixing-length eddy viscosity should be used instead to circumvent this problem. The resolutions in wall units for their simulation were ($s^+ \approx 60$) and ($l^+ \approx 30$), where the first off-wall node in the wall normal direction was located in the lower edge of the logarithmic layer. A different approach to solving the wall modeling issues is by hybrid RANS/LES techniques. Instead of using a refined subgrid, the steep wall normal gradients are resolved by the

grid, i.e. by using a low Reynolds grid. Compared to wall resolved LES the directions parallel to the wall will not be resolved. Thus, the near-wall structures are not resolved and the SGS model must be modified in this region to account for these unresolved motions. A possibility is to augment the SGS model with an ordinary RANS eddy viscosity model in the wall region. The fundamental idea is that the governing RANS equations are very similar to the LES equations except for the definition of the turbulent viscosity, as pointed out by Davidson and Dahlström [27]. The turbulent viscosity is proportional to a characteristic turbulent length and velocity scale, which are defined in different ways for RANS and LES. This type of technique can further be divided into two different categories based on the interface condition. Zonal methods refer to methods in which the interface is defined in advance and often in terms of wall units, while universal models have the inherent ability to switch between the two domains. For these techniques the crucial point seems to be how to transfer modeled turbulence from the RANS region to resolved stresses as boundary conditions to the LES domain. A direct consequence of the above described approach is that the near-wall solution will never be better than the embedded RANS model.

Two trends can be identified over the years for the zonal techniques. First, several studies aimed at embedding more physics in the RANS model and, second, investigations have been made of the RANS/LES interface position and rigidity. The studies have in their simplest form implemented one-equation models [27] to two-equation models [33–36]. Lately, efforts have been made to introduce true or synthetic fluctuations over the RANS/LES interface. The idea is to circumvent the poorly resolved stresses from the RANS region (Davidson and Dahlström [27]) and introduce either true turbulent fluctuations from a DNS over the interface or introduce synthesized turbulent fluctuations [37]. An even more refined technique for improving the interface condition was evaluated in Nicoud et al. [26]. They used suboptimal control theory for the turbulent channel flow to force the outer LES solution towards a desired solution by using the wall stress boundary condition as a control. The drawback was that the computational cost for the channel flow was 20 times greater than for an explicit wall stress model.

In the final class of wall modeling techniques, ”universal models”, as proposed by Labourasse and Sagaut [38], will be discussed. Universal

models are models that inherently switch between RANS and LES mode and apply the same equations in both regions. The most commonly used method is the DES simulation technique used first by Spalart et al. [39]. In DES the same equations are solved for both the RANS and LES zones by using a simple one-equation model for the modified turbulent viscosity close to the wall. When the grid in all directions is much smaller than the boundary layer thickness, it smoothly turns to an SGS model. The essence of the model is the recognition of the DES length scale, $\widetilde{l}$, defined as

$$\widetilde{l} = \min(d_w, C_{DES}\Delta) \tag{3}$$

The DES length scale actually consists of the evaluation of two different length scales. The first RANS length scale, d_w, is based on the distance to the closest wall and the LES length scale, $C_{DES}\Delta$, depends on the grid spacing. The LES length scale, $\Delta = \max(\Delta x, \Delta y, \Delta z)$ and C_{DES} is the model constant, $C_{DES} = 0.65$, obtained from isotropic decaying turbulence. The two length scales will converge over the RANS/LES interface and contribute to a smooth transition between the zones. In contrast to the zonal models the approach has no issues of discontinuities in any variable over the zones. This is also one of its drawbacks because, in its basic form, it covers the whole boundary layer in the RANS mode. The grid dependency of the method has however one attractive aspect. With increased grid refinement, the model gradually turns the DES toward LES and in the end toward DNS, even though this was not the primary aim of the model. However, too high a wall parallel resolution can locally activate the LES mode close to wall, causing a premature or "grid-induced" separation. This makes grid generation an even more delicate task than in the case of LES and makes the method sensitive to cells with low aspect ratios. The method aims at industrial applications at high Reynolds numbers, and promising results have been presented for several complex geometries and flow fields [3,8,10–13,23,40]. A similar technique that circumvents the grid dependency is the Scale Adaptive Simulation (SAS) model pioneered by Menter [41, 42]. The model uses, as compared to DES, a dynamic length scale based on locally resolved eddies in the flow. This length scale is defined as:

$$L_{vK} = \sqrt{\frac{\frac{\partial U_i}{\partial x_j}\frac{\partial U_i}{\partial x_j}}{\frac{\partial^2 U_l}{\partial x_m^2}\frac{\partial^2 U_l}{\partial x_n^2}}} \tag{4}$$

The length scale evaluated in Eq. 4 is based on second velocity derivatives that are numerically difficult to estimate with decent accuracy and implicitly require a fundamental understanding of both grid refinement and numerical methods, which in some senses can be more difficult to control than the grid issues in DES, where the user has greater control. The method is still in its infancy and has so far only been evaluated for a minor number of flow fields. Both DES and the SAS model have however been evaluated for circular cylinders (Travin et al. and Menter et al. [8,41]) and have shown similar results in terms of the surface pressure distribution. Other techniques categorized together with the universal models include that presented by Speziale [43], who used blending of the stress tensor in a Reynolds stress model, which makes it possible to smoothly transfer between RANS and LES. This idea was further developed in Batten el al. [44, 45] and was called the Limited Numerical Scale (LNS), where a parameter-free definition of the blending function based on products of turbulent length and velocity scales was used. In essence, the LNS approach identifies the resolved and unresolved fractions of the kinetic energy. The technique was also used for subdomain simulations involving RANS and LES and was then referred to as ”embedded LES” through a forcing over the LES/RANS interface using synthetic turbulence, similar to the zonal methods described above.

It can be concluded from the discussion above that all techniques presented have drawbacks that can be more or less critical for complex flows. In the present paper the DES modeling technique was chosen for two reasons: the first and most obvious is that the methods available in the present version of FLUENT are restricted to DES and equilibrium wall functions. Secondly, the DES model has successfully been applied to similar objects and flow fields.

4 Numerical approach

The object used in the present simulation is the generic side mirror mounted on a flat plate. It consists of a half cylinder with the diameter $D = 0.2$ [m] and height $H = D$ blunted by a quarter sphere on top, which gives a total height of $H = 1.5D$. The geometry is shown in Fig. 2 and its position on the plate is represented in Fig. 3. The Reynolds number based on the mirror diameter is $Re_D \approx 5.2 \cdot 10^5$ with a freestream velocity of 39 [m/s]. This freestream velocity results in a Mach number of 0.11. There are no indications that compressible effects or sound wave reflections have a prominent role in the present flow field, which implies that an incompressible approach should be justified.

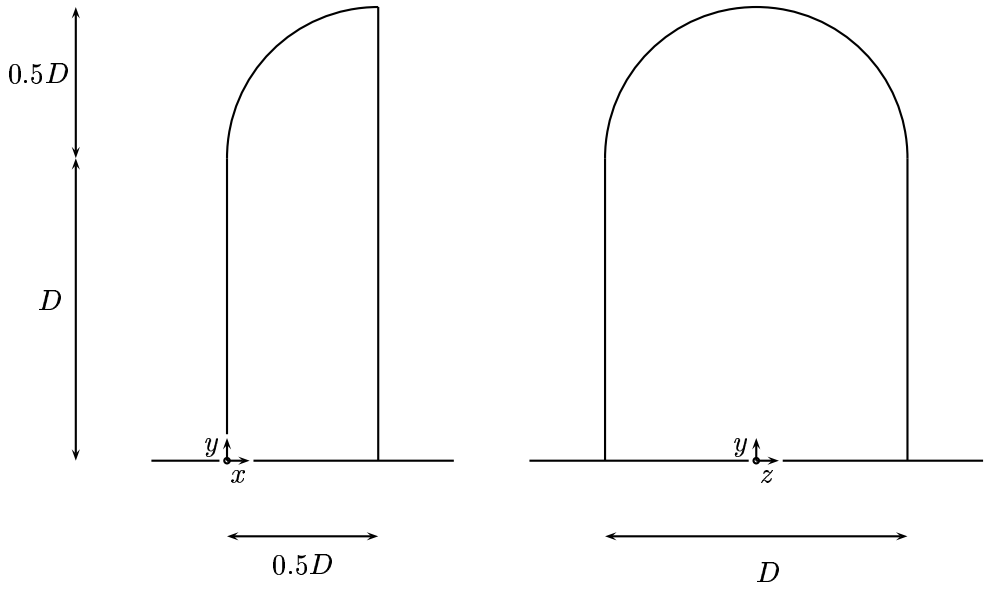

Figure 2: Mirror geometry; side view and front view, respectively

The code used in this paper is the unstructured FLUENT 6.2 commercial solver. It is based on a control volume formulation to convert the governing equations to a solvable set of algebraic equations. The code in the present state uses a collocated scheme with cell-centered storage of both scalars and vectors. In the present paper, the incompressible segregated solver is used with an implicit SIMPLEC pressure-velocity coupling algorithm. A second-order, upwind-biased scheme is used for the convective fluxes over the whole domain. The discretization in time follows an implicit second-order scheme to obtain a converged solution, and convergence is defined as when the residuals have dropped three orders of magnitude each time step for the solved variables. The computational domain is built up of a block-structured hexahedral mesh in ICEM 5.1 and consists of $N_{xyz} \approx 5.83 \cdot 10^6$ cells. The domain is bounded by an inlet $15D$ upstream of the mirror and an outlet $30D$ downstream of the mirror. In the spanwise extension the far field boundaries are positioned $15D$ on opposite sides of the mirror. In the plate normal direction a far field boundary is located $15D$ above the plate.

The inlet boundary condition follows the "trip-less" approach, with an initial steady state inlet turbulence intensity of 0.1% and a turbulent inlet length scale of $0.5D$ followed by a zero inlet turbulent viscosity. Other boundary conditions used in the present work are a pressure boundary condition at the outlet and symmetry boundary conditions at the far field boundaries. No-slip boundary conditions are used over the plate and mirror geometry.

The simulation procedure was as follows: a converged RANS solution based on the S-A model served as an initial condition. After this initialization, the inlet turbulent viscosity was set to zero and a coarse time step was first chosen to convect freestream disturbances downstream. The time step at this stage was $\Delta t = 1 \cdot 10^{-3}$[s] $(= \alpha D/U)$, and the simulation was run for $19.5D/U$. This means that a perturbation at the inlet travels a distance of 19.5D downstream or 4D downstream the mirror. The time step was then reduced to $\Delta t = 2 \cdot 10^{-5}$[s] $(= \beta D/U)$ and run for an additional $78D/U$, which corresponds to an additional 1.7 full domain flow-throughs. After a total simulation time of $97.5D/U$, extraction of statistics and wall pressures was initiated and the simulation was run for a further $78D/U$. The sampling frequency of the wall pressure was 50[kHz], which corresponds to sampling at each time step.

The Strouhal number for cylinders and spheres is typically $St \approx 0.2$, which results in a fundamental frequency of $f_n = 40$[Hz] with the periodicity $T_p = 4.88D/U$. The Strouhal number is defined as $St = fD/U$, where f is the frequency, U is the freestream velocity and D is the mirror diameter. The time during which statisitics is extracted will contain 16 periods of this fundamental frequency, which might be insufficient for a proper description of the flow statistics for the lowest frequencies.

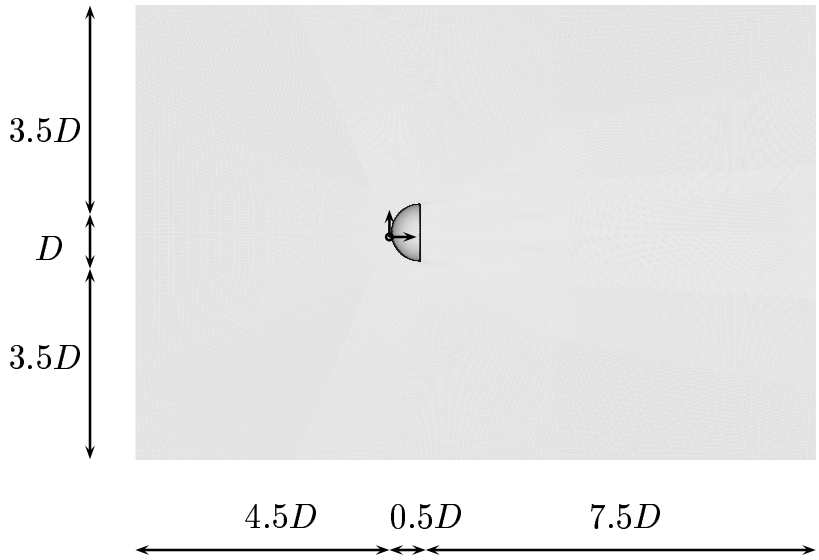

Figure 3: Mirror and plate, xz-plane

The suction side of the mirror is resolved by 7900 cells with 105 nodes over the mirror height and 55 cells over the mirror width. The first off-wall node close to the mirror trailing edge is located at $\Delta y = 2{\cdot}10^{-2}$[mm] in the wall normal direction, and this distance is successively increased when approaching the upstream stagnation point. As an estimate of the boundary layer thickness, a laminar Blasius solution for the cylinder flow was used [20]. At a Reynolds number of $Re_D = 5.2 \cdot 10^5$, the estimated boundary layer thickness, $\delta_{R=0.1} \approx 0.59$[mm], is resolved by 10 cells in the wall normal direction. To prevent an eventual grid-induced separation in RANS mode, the following relation must be ful-

filled, Menter et al. [41]:

$$C_{DES}\Delta = \mathcal{O}(1)\delta \tag{5}$$

In Eq. 5, Δ is the maximum extension of the cell and δ is the boundary layer thickness. For the cells located over the suction side close to the trailing edge, this requirement is fulfilled by at least one order of magnitude.

5 Flow field results

This section gives flow field results for the simulation. The results are further divided into mean and instantaneous results, followed by the time-dependent results.

5.1 Mean and instantaneous results

In this section n^+ will refer to the wall normal direction, s^+ to the streamwise direction and l^+ to the lateral direction. The n^+ values over the suction side range from $0.19 < n^+ < 5.4$, with a mean value of $\overline{n^+} = 1.8$. Over the plate, the n^+ values range from 0.8 to 410, where the maximum values occurs close to the leading edge of the plate and the lower limit values typically occur in the mirror wake. The n^+ levels over the plate and mirror rear side are also shown in Fig. 4. The log-law is applied for cell centroids located in the range of $30 < n^+ < 300$ and the viscous sublayer is assumed to be resolved for cell centroids located at $n^+ < 5$. An attempt to resolve the boundary layer over the plate would increase the amount of cells necessary beyond the limit of available computer resources. The log-law is therefore assumed to be valid over a major part of the plate while resolving the viscous sublayer over the suction side of the mirror. The s^+ is typically $34 - 37$ on the suction side of the mirror close to the trailing edge and the corresponding l^+ value varies between 130 and 150 for the same locations.

The CFL number ranges from $0.0014 < CFL_{conv} < 2.85$ where the maximum value typically occurs close to the mirror trailing edge and is limited to just a few cells.

Figure 5 shows the location of the RANS/LES switch over the $z = 0$ plane. A close-up view over to the trailing edge is seen in Fig. 5(b)

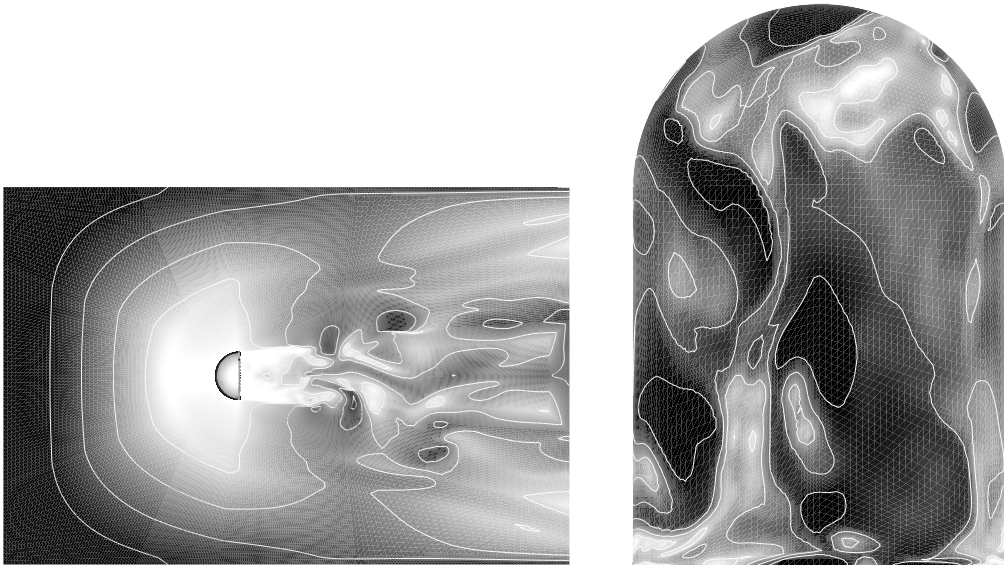

(a) Contour levels of n^+ over the plate at $\langle 1, 75.8, 150.5, 225.2, 300\rangle$

(b) Contour levels of n^+ over the mirror pressure side at $\langle 1, 3.2, 5.5, 7.8, 10\rangle$

Figure 4: Contours of n^+ over the plate and the mirror pressure side respectively

together with superimposed velocity vectors. As discussed above, the boundary layer is completely captured within the RANS domain even though the s^+ and l^+ are significantly lower than what is customary for a low Reynolds RANS grid.

In Fig. 6 the normalized wall shear stress, C_τ, is presented for three cut planes over the suction side of the mirror and compared with measurements over both a sphere and a cylinder [46, 47]. The normalized wall shear stress is defined as

$$C_\tau = \frac{\tau}{\rho U^2} Re^{0.5} \tag{6}$$

which is appropriate for laminar boundary layers. Over the $y = 0.5D$ plane the flow over the suction side is typically two dimensional and

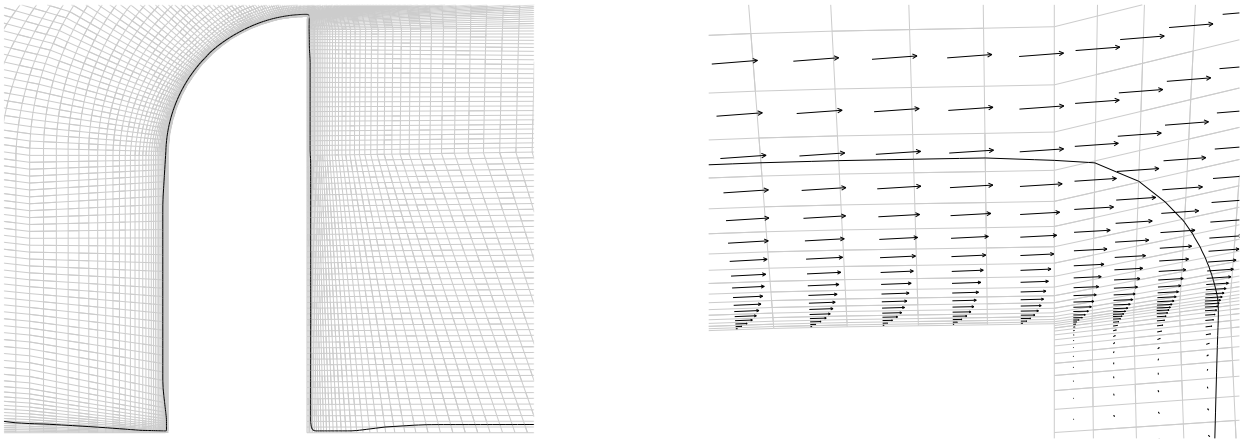

(a) Grid and location of the RANS/LES switch

(b) Close-up view of velocity vectors and location of the RANS/LES switch close to the trailing edge

Figure 5: Location of the RANS/LES switch over plane $z = 0$

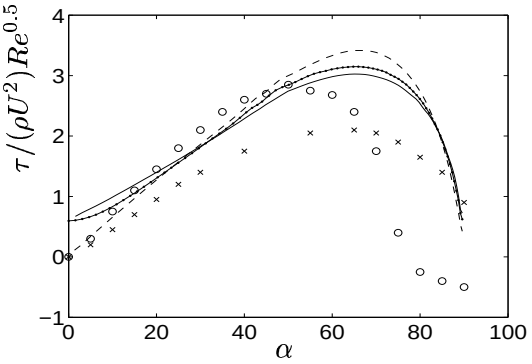

Figure 6: Normalized wall shear stress over suction side, $(-)$ Symmetry line, $(--)$ $y = 0.5D$, $-.-$ $y = D$, $(\times)$ Exp. over a sphere at $Re = 3.18 \cdot 10^5$,(o) Exp. over a cylinder at $Re = 1 \cdot 10^5$

corresponds well to the cylinder experiment up to 50^o, where the measured wall shear stress drops drastically. The other two cut planes are located at $z = 0$ and at $y = D$. At these locations the flow over the mirror is three dimensional with stagnation further upstream, which makes a direct comparison with both the cylinder and sphere measurements difficult. Both the cylinder and the sphere have well defined stagnation points at $\alpha = 0^o$, where the generic side mirror shows an expected overprediction in the wall shear stress. Even though the simulation overpredicts the wall shear stress at $\alpha = 0^o$, the curves converge rapidly with the cylinder measurements, possibly due to an overproduction of the turbulent viscosity. Further downstream an underprediction of the simulated wall shear stress can be identified in the range ($20^o < \alpha < 50^o$). That an excessive production of turbulent viscosity causes the discrepancy in the results is verified in Fig. 7(a), which shows an iso-surface for $\nu_t/\nu = 10$. Compared to the existing side mirror measurements, the laminar separation should occur close to the $\nu_t/\nu = 10$ iso-surface. The high ν_t prevents the laminar separation to be captured.

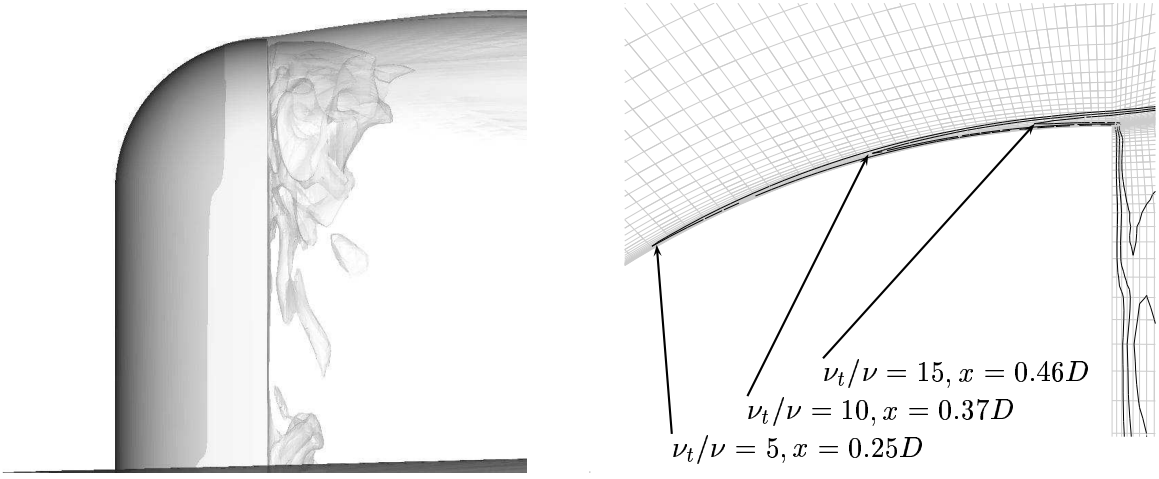

(a) Turbulent viscosity ratio, $\nu_t/\nu = 10$

(b) Turbulent viscosity ratio over plane $z = 0$

Figure 7: Contours of the turbulent viscosity ratio

In Fig. 8 the mean pressure coefficient over the mirror is compared to the corresponding Daimler Chrysler measurements [21]. The mean pressure show good agreement with the measured results except at the sensors located near the upstream separation line (S10, S25), where the simulation underpredicts the mean pressure. A complete description of the monitor positions is given in Table B in Appendix B and this is visually presented in Fig. 9.

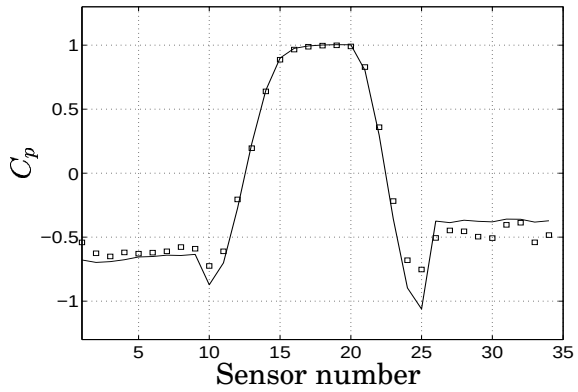

Figure 8: Mean pressure over mirror, (o) experiment and (-) simulation

Figure 10 is a vorticity snap-shot of two cut planes. These cut planes clearly show the presence of two major structures dictating the low frequency flow conditions in the mirror wake. The first structure impinges the plate at approximately $1.5D$ from the rear side of the mirror with a length scale comparable with the mirror height, Fig. 10(b). A second, more strongly alternating structure occurs in the plate parallel plane $1D$ downstream of the mirror, as seen in Fig. 10(a). The interaction between these structures has a major impact on the pressure fluctuations which are responsible for the major part of the generated sound.

5.2 Time dependent results

Contrary to both the cylinder and sphere flow no strong fundamental frequency could be observed over the conducted simulation, as can be understood in Fig. 11.

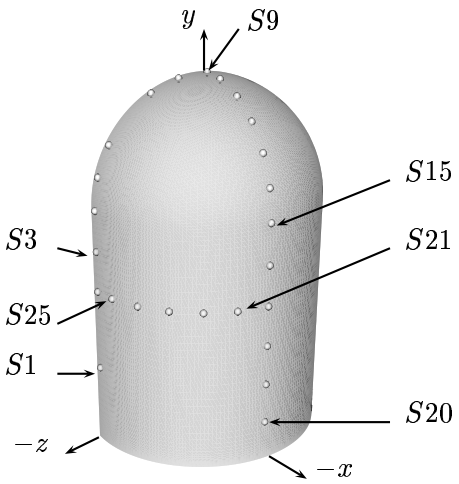

(a) Monitor distribution over the suction side

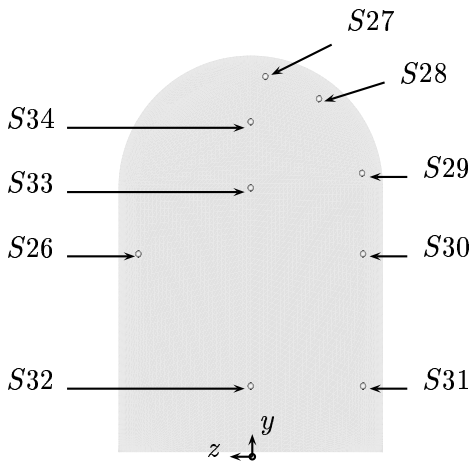

(b) Monitor distribution over the pressure side, rear view

Figure 9: Location of surface sensors over mirror pressure and suction side respectively

The amplitudes of the oscillations in the force coefficient are similar to the findings in the sphere simulations presented in Constantinescu et al. [13] but show a higher content of lower frequencies. It is also clear in the figure that lower frequencies than the fundamental frequency exist in the present flow field. Both the sphere and cylinder are known for their modulation in the force coefficient, and this can be the cause of the appearance of the force coefficient. In either case, additional studies should include a longer time sequence to improve statistics. The large variations in the force coefficient are caused by the resolved structures in the recirculation zone behind the mirror. This is apparent in Fig. 12(a) where the rms of the pressure is presented over both the suction and pressure sides of the mirror. The contours over the pressure side are highly asymmetric, with the highest levels below $1D$ of the mirror height.

Figure 12(b), which gives the rms of the pressure fluctuations over the plate, shows that the alternating structures and their upstream

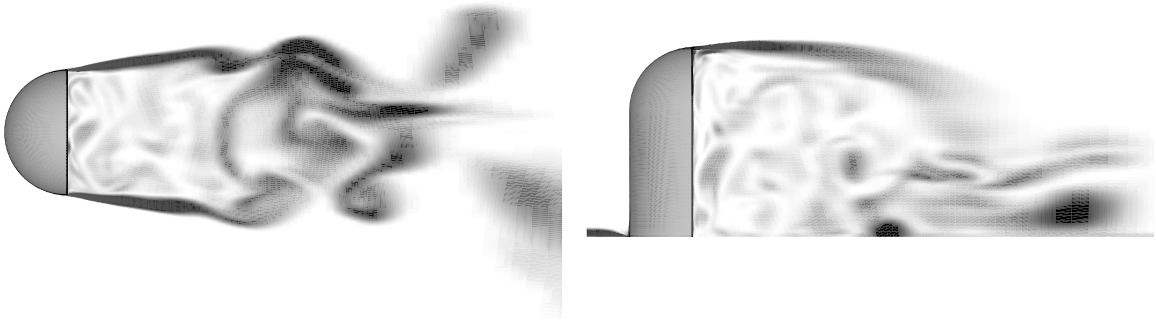

(a) Plane, $y = 0.5D$ (b) Plane, $z = 0$

Figure 10: Snapshot of vorticity magnitude

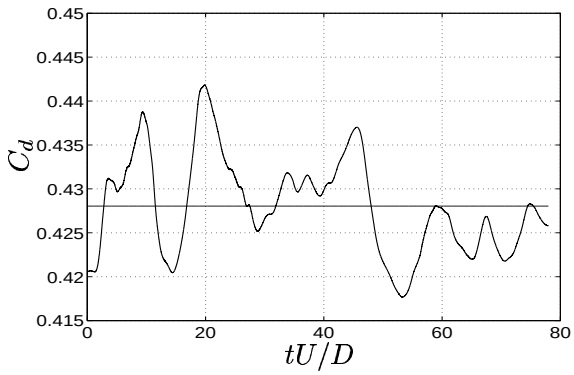

Figure 11: Instantaneous drag coefficient and mean drag over the mirror

shear layers are the dominating sources of the sound generation. In comparison to Fig. 12(a) the rms levels of the pressure fluctuations are almost 10 times as large. The transversal structures identified in Fig.

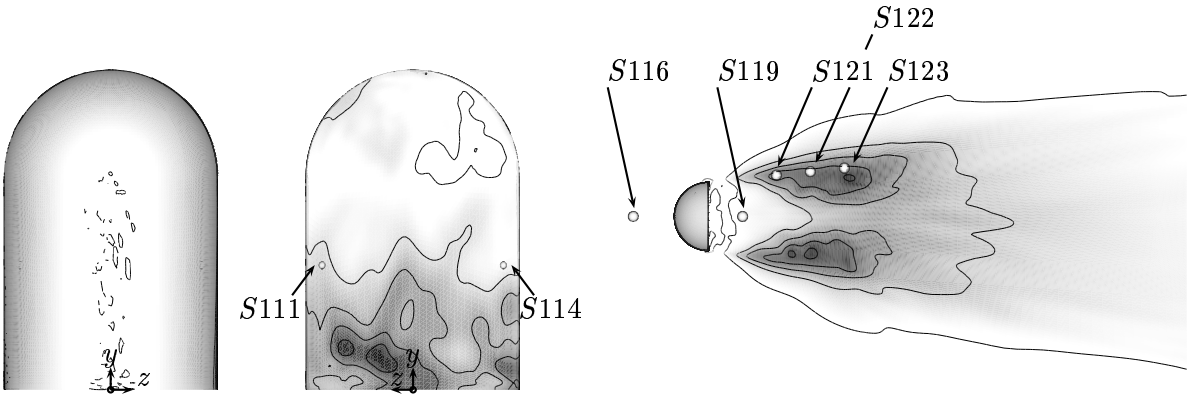

(a) RMS of pressure on mirror suction and pressure side respectively, $10 < p_{rms} < 35$

(b) RMS of pressure fluctuations over the plate ranging from $20 < p_{rms} < 250$ and contours at $\langle 20, 77.5, 135, 192.5, 250 \rangle$

Figure 12: RMS of wall pressure over mirror and plate respectively

10(b) increase the three dimensionality by interacting with the alternating side structures, thus increasing the downstream levels of pressure fluctuations over the plate.

Next, fluctuations over the pressure sensors are presented in the frequency plane. The location of the sensors is given in Table B in Appendix B and in Fig. 12 and the predictions are compared with the Daimler-Chrysler measurements [3].

Analyzing discontinuous signals in the frequency plane is always a controversial matter, especially when the time sequence appears to be insufficient. For acoustic measurements the standard procedure is approximately seven seconds of sampled data to obtain converged statistics, which is not feasible in simulations of the kind presented in this paper. Here, Fourier transformation of the autocorrelation was used to obtain the power spectrum. The wish to minimize the frequency leakage when truncating discontinuous signals and the energy preservation of the lowest frequencies make this approach the most appropriate choice.

The fluctuating pressure level presented in the figures is computed in the following way

$$PL = 10log_{10}\frac{\hat{p}}{p_{ref}^2} \tag{7}$$

where $p_{ref} = 2 \cdot 10^{-5}$ is the reference pressure. The presentation of hydrodynamic pressure fluctuations in terms of SPL can be somewhat misleading as sound pressure levels only account for emissions in the intermediate and far field. For this reason, the fluctuating hydrodynamic pressure levels (PL) are presented instead.

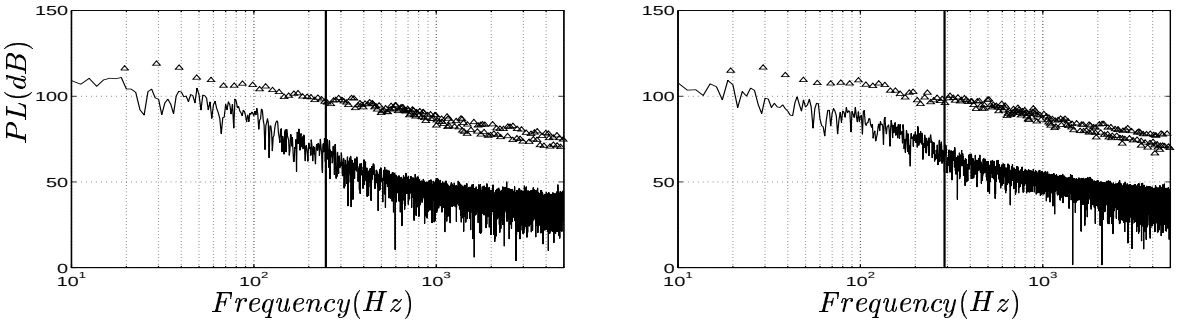

(a) PL at surface sensor no. 111

(b) PL at surface sensor no. 114

Figure 13: PL of wall pressure over sensors S111 and S114

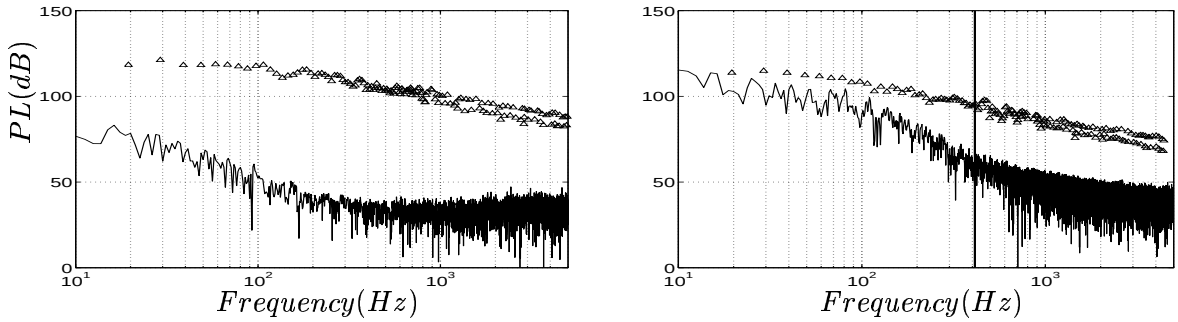

(a) PL at surface sensor no. 116

(b) PL at surface sensor no. 119

Figure 14: PL of wall pressure over sensors S116 and S119

The results collected from the two sensor points located on the pressure side of the mirror opposite to the symmetry plane are presented in Fig. 13. The experiments for these two sensors show a high degree of

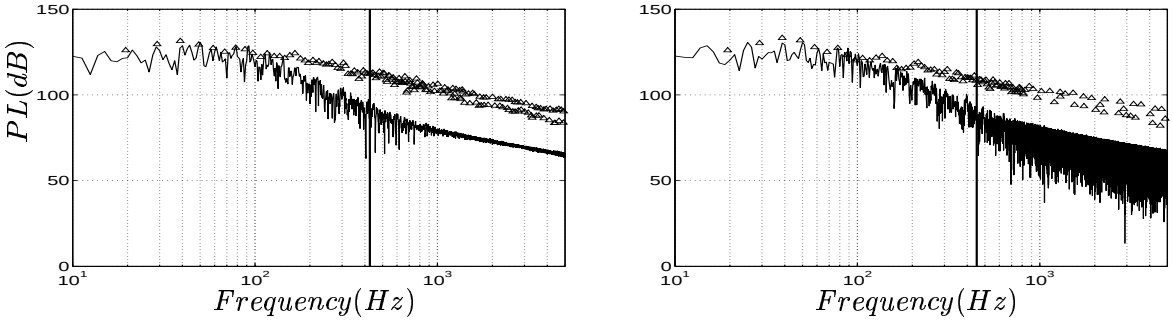

(a) PL at surface sensor no. 121

(b) PL at surface sensor no. 122

Figure 15: PL of wall pressure over sensor S121 and S122

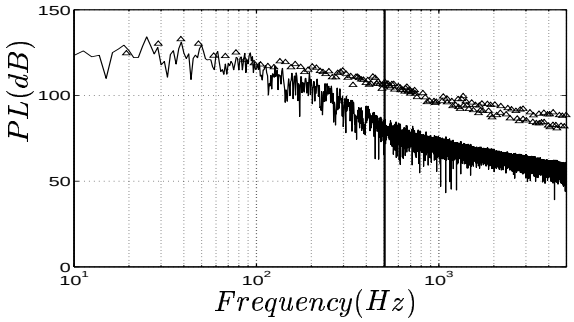

(a) PL at surface sensor no. 123

Figure 16: PL of wall pressure over sensor S123

symmetry with a maximum peek at 30 Hz. Furthermore, all frequencies except possibly at 20 Hz are significantly underpredicted in the present simulation, which is rather annoying. This underprediction may be a consequence of the misrepresentation of the upstream flow state or the too short simulation time and should be investigated further. An asymmetry for the lowest frequencies in the simulation results can also be observed that is most probably due to too short a simulation time. However, the fluctuating pressure levels over the pressure side of the mirror,

as pointed out in the text above, is almost an order lower than the findings downstream of the plate. Sensor S116 positioned in the upstream boundary layer of the mirror is also poorly predicted. This is expected since it is located in the unresolved plate boundary layer. Sensor S119 positioned $0.5D$ downstream of the mirror geometry is shown in Fig. 14. Compared to the sensors over the pressure side of the mirror the agreement is significantly better up to 100 [Hz], where the pressure level drops rapidly with increasing frequency. The experiments show for this position a lower tonal contents as compared to sensors S111 and S114. The last three sensors, S121 to S123, are positioned in the high fluctuating pressure level region in the wake. Good agreement is found up to 200 [Hz], where almost all of the lower frequencies are correctly captured. The fundamental frequency of 40 [Hz] can be identified for this region. Studying the results from the pressure fluctuations above, a general conclusion is that there seem to be resolution issues above 200 [Hz]. An attempt to compute the mesh cut-off frequencies was made to analyze this further. The mesh cut-off frequency can be estimated as $f_{max} = |u_{rms}|/(2\Delta x)$, where u_{rms} is the rms of the resolved fluctuating velocity magnitude and Δx is the grid spacing. The estimated mesh cut-off frequency for the first off-wall cell is summarized in Table 1.

Cut-off frequency for first off-wall cells			
Sensor	$\|u_{rms}\|$	$2\Delta x$	f_{max}
S119	8.17	0.01792	413
S121	11.75	0.0238	426
S122	12.99	0.0238	451
S123	14.8	0.0238	504

Table 1: Mesh cut-off for four of the surface sensors

The analysis only treats the cut-off that is caused by the mesh and represents a measure of the highest possible frequency according to the Nykvist criterion; the mesh cut-off for each sensor is also marked by a line in Figs. 13 to 16. However, the results serve as an engineering tool to estimate the mesh cut-off, and it is clear that to improve the results in the high frequency region, a significantly larger number of cells is needed in the wake region unless no improvement of the discretization

scheme is made.

6 Acoustic results

The sound emission at five observer points was computed and compared with experimental data. The positions of the observers are given in Table B in Appendix B and are shown in Fig 17. The storage of the two source terms contributes to 5GB of data for the present simulation and the treatment of additional volume sources is simply not feasible. The sound emission results are presented in Figs. 18(a) to 18(e). It can be seen in the experimental results for the first four observers that the spectral content is almost identical. The best agreement between experiments and simulation is obtained for observers M10 and M11, Figs. 18(c) and 18(d). These two observers are located above the region with high fluctuating pressure levels.

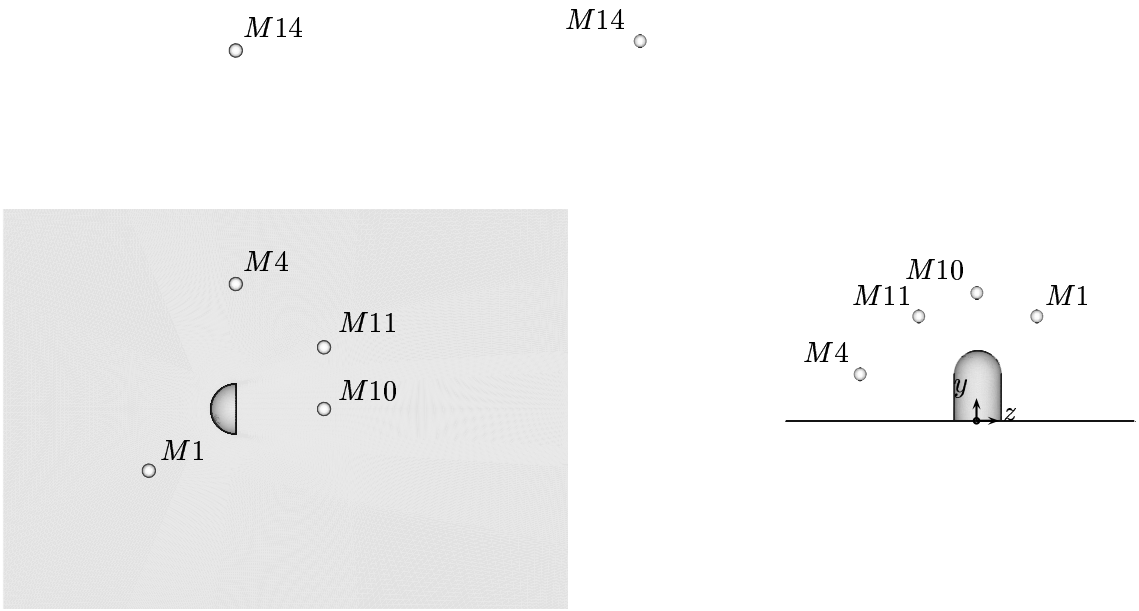

Figure 17: Microphone positions, top and front view respectively

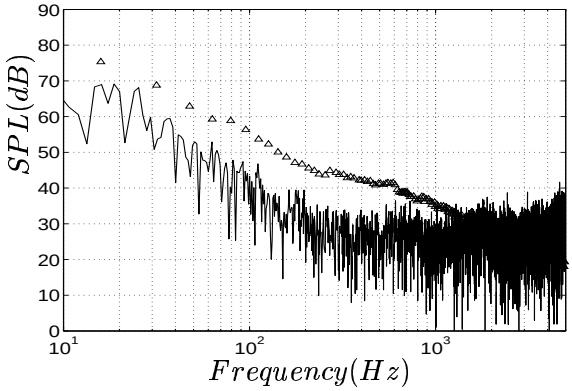

(a) SPL at microphone no. 1

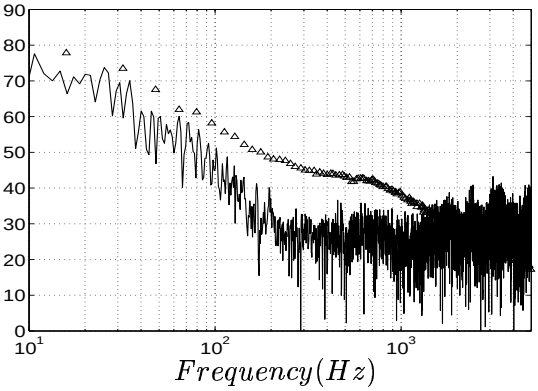

(b) SPL at microphone no. 4

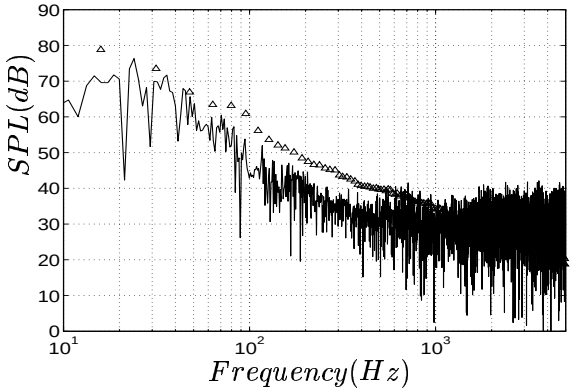

(c) SPL at microphone no. 10

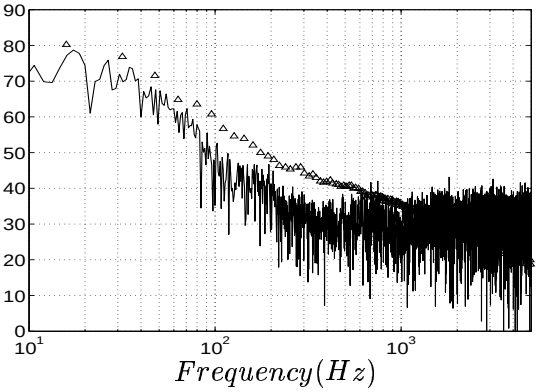

(d) SPL at microphone no. 11

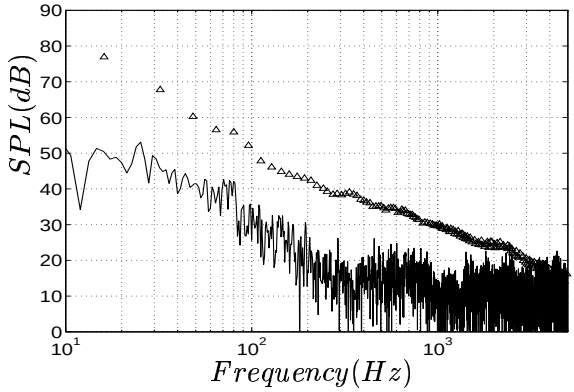

(e) SPL at microphone no. 14

Figure 18: SPL at observers

For observer M1, located upstream of and above the mirror, the simulation result clearly underpredicts the measurements, Fig. 18(a). This is expected owing to the neglection of volume terms as well as the unresolved plate boundary layer in the simulation. In Fig. 18(b) the observer M4 is positioned in the plane of the rear side of the mirror, $1D$ above the plate. This observer is located close to the high fluctuating pressure region over the plate and an improvement in SPL for this observer is found compared to observer M1. The directional vector from this high fluctuating pressure level region on the plate and the observer is significantly deviating from the wall normal, resulting in a low projected area for these wall sources. Again, neglecting the quadrapole terms as well as the unresolved plate boundary layer may be the cause to some of the discrepancy in sound pressure levels. This discrepancy in results increases when the observer is located even further away from the object, Fig. 18(e).

7 Conclusions and future work

In this paper a first attempt is made to predict both the flow field and emitted sound past a generic side mirror mounted on a flat plate. The Reynolds number is $5.2 \cdot 10^5$ based on mirror diameter; the corresponding Mach number for this flow field is $Ma = 0.11$. Owing to the low Mach number, the flow field is solved on the basis of an assumption of incompressibility. Previous experiments have shown the presence of a pressure induced laminar separation upstream of the suction side of the mirror and no published simulation has yet been able to capture this phenomenon.

The present simulation attempts to capture this flow field by an approach first presented by Shur et al. The technique basically consists of two steps. An initial flow field is first obtained with turbulence levels over the whole domain. The inlet boundary condition is then shifted to a level of zero turbulence over the inlet, and the turbulence is successively swept out of the domain during the time marching. With this technique the wake will contain self-sustained levels of turbulence which will diffuse to the upstream boundary layers. Still, this technique results in a turbulent to physical viscosity ratio of 10 close to the point where the separation should occur and is still too high to capture a laminar sepa-

ration.

The radiated sound is calculated from the Ffowkes-Williams and Hawkings analogy, where the two terms treated are the instantaneous fluctuating pressure and its temporal derivative. Thus, two major assumptions are made. First, quadrapole terms are neglected and secondly the simulation is conducted in an incompressible manner, which neglects any sound wave reflection. The overall conclusions drawn from the present simulation are as follows.

- Even though the simulation fails to predict the laminar separation, good agreement is found between simulated and experimental results for the sensor points positioned most downstream up to 100 Hz.
- Large discrepancies are found for the intermediate and far field observers, possibly because of the neglected volume sources and the unresolved plate boundary layer.
- The simulation time should be increased to gain better statistics in the wake and force coefficients.
- The levels of the surface pressure fluctuations fall rapidly above 200Hz for all the sensors of interest. These predictions can be improved by using a more isotropic wake mesh and a less dissipative discretization scheme and to some extent even a less dissipative turbulence model.
- A proper representation of the upstream laminar separation can also improve the intermediate frequency range.

A recurrent drawback in the present simulation is the short simulation time, which will be increased significantly in future studies. A further study is proposed where the turbulent viscosity will be set to zero upstream of the mirror in order to capture the laminar separation.

8 Acknowledgments

This work was supported by the Volvo Car Corporation and the Swedish Agency for Innovation Systems (VINNOVA). I also would express my

gratitude toward Dr. Franz R. Klimetzek at Daimler Chrysler, who let me use their experimental data.

References

[1] R. Höld, A. Brenneis, and A. Eberle. Numerical simulation of aeroacoustic sound generated by generic bodies placed on a plate: Part I - prediction of aeroacoustic sources. In *5th AIAA/CEAS Aeroacoustics Conference. Seattle, Washington*, pages AIAA–99–1896, 10-12 May 1999.

[2] R. Siegert, V. Schwartz, and J. Reichenberger. Numerical simulation of aeroacoustic sound generated by generic bodies placed on a plate: Part II - prediction of radiated sound pressure. In *5th AIAA/CEAS Aeroacoustics Conference. Seattle, Washington*, pages AIAA–99–1895, 10-12 May 1999.

[3] T. Rung, D. Eschricht, J. Yan, and F. Thiele. Sound radiation of the vortex flow past a generic side mirror. In *8th AIAA/CEAS Aeroacoustics Conference. Breckenridge, Colorado*, pages AIAA–2002–2340, 17-19 June, 2002.

[4] EXA Consortium. Vaildation update: Model mirror. Aeroacoustic Consortium 2003/2004 Presentation, 20 August, 2003.

[5] L. Bipin, S. Sandeep, and X. Jieyong. Computational aeroacoustic analysis of a generic side view mirror. In *Noise and Vibration Conference and Exhibition. Traverse City, Michigan*, pages SAE–2003–01–1698, 5-8 May, 2003.

[6] J.E. Ffowcs Williams and D.L. Hawkings. Sound generation by turbulence and surfaces in arbitrary motion. *Philos. Trans. Roy. Soc.*, A 264 No. 1151:321–342, 1969.

[7] K.S. Brentner and F. Farassat. Modeling aerodynamically generated sound of helicopter rotors. *Prog. Aerospace Sci.*, 39:83–120, 2003.

[8] A. Travin, M. Shur, M. Strelets, and P Spalart. Detached-eddy simulations past a circular cylinder. *Flow, Turbulence and Combustion*, 63:293–313, 1999.

[9] M. Strelets. Detached eddy simulation of massively separated flows. In *39th AIAA Aerospace Sciences Meeting and Exhibit. Reno, NV*, pages AIAA–2001–0879, 8-11 January, 2001.

[10] V.N. Vatsa and B.A Singer. Evaluation of a second-order accurate Navier-Stokes code for detached eddy simulation past a circular cylinder. In *21th AIAA Aerospace Sciences Meeting and Exhibit. Reno, NV*, pages AIAA–2001–0879, 8-11 January, 2001.

[11] S. Schmidt and F. Thiele. Detached eddy simulation of flow around A-airfoil. *Flow, Turbulence and Combustion*, 71:261–278, 2003.

[12] G.S. Constantinescu and K.D. Squires. LES and DES investigations of turbulent flow over a sphere at Re=10000. *Flow, Turbulence and Combustion*, 70:267–298, 2003.

[13] G.S. Constantinescu and K.D. Squires. Numerical investigations of flow over a sphere in the subcritical and supercritical regimes. *Physics of Fluids*, 16:1449–1466, 2004.

[14] M. Shur, P. Spalart, M. Strelets, and A. Travin. Navier-Stokes simulation of shedding turbulent flow past a circular cylinder and a cylinder with backward splitter plate. In *Computational Fluid Dynamics '96, Proceedings of the Third ECCOMAS Computational Fluid Dynamics Conference*, pages 676–682, 9-13 September, 1996.

[15] P. Spalart. Strategies for turbulence modelling and simulations. *International Journal of Heat and Fluid Flow*, 21:252–263, 2000.

[16] N. Curle. The influence of solid boundaries upon aerodynamic sound. *Proc. Roy. Soc*, A231:505–514, 1955.

[17] J. Ask and L. Davidson. An acoustic analogy applied to the laminar upstream flow over an open 2D cavity. *In press, C.R. Mecanique*, 2005.

[18] J. Ask and L. Davison. An investigation of outlet boundary conditions for incompressible near field acoustics. In *11th AIAA/CEAS Aeroacoustics Conference*, pages AIAA–2005–2992, 23-25 May, 2005.

[19] J. Larsson. Computational aero acoustics for vehicle applications. Chalmers University of Technology, 2002.

[20] H. Schlichting. *Boundary Layer Theory*. Springer, 1969.

[21] F. Klimetzek. Personal communication. Daimler-Chrysler, Research and Technology, Advanced Concepts (RBP/BC), Sept, 2005.

[22] P. Spalart, L. Hedges, M. Shur, and A Travin. Simulation of active flow control on a stalled airfoil. *Flow, Turbulence and Combustion*, 71:361–373, 2003.

[23] L.S. Hedges, A.K. Travin, and P. Spalart. Detached-eddy simulations over a simplified landing gear. *Journal of Fluids Engineering*, 124:413–423, 2002.

[24] DR. Chapman. Computational aerodynamics development and outlook. *AIAA Journal*, 17:1293–1313, 1979.

[25] L. Temmerman, M. Hadziabdic, M.A. Leschziner, and K. Hanjalic. A hybrid two-layer URANS-LES approach for large eddy simulation at high reynolds number. *International Journal of Heat and Fluid Flow*, 26:173–190, 2005.

[26] F. Nicoud, J.S. Baggett, P. Moin, and W. Cabot. Large eddy simulation wall-modeling based on suboptimal control theory and linear stochastic estimation. *Physics of Fluids*, 13(10):2968–2984, 2001.

[27] L Davidson and Dahlström. Hybrid LES-RANS: An approach to make LES applicable at high Reynolds number. In *ICHMT International Symposium on Advances in Computational Heat Transfer*, 2004.

[28] C.D. Wilcox. *Turbulence modeling for CFD; Second edition*. DCW Industries, 1998.

[29] T.J. Craft, S.E. Gant, H. Iavocides, and B.E. Launder. A new wall function strategy for complex turbulent flows. *Numerical Heat Transfer*, B(45):301–318, 2004.

[30] E. Balaras and C. Benocci. Two-layer approximate boundary conditions for large-eddy simulations. *AIAA Journal*, 34(6):1111–1119, 1996.

[31] W. Cabot and P. Moin. Approximate wall boundary condition in the large-eddy simulation of high Reynolds number flow. *Flow, Turbulence and Combustion*, 63:269–291, 1999.

[32] M. Wang and P. Moin. Dynamic wall modeling for large-eddy simulation of complex turbulent flows. *Physics of Fluids*, 14(7):2043–2051, 2002.

[33] L. Davidson and S.H. Peng. Hybrid LES-RANS modeling: A one equation SGS model combined with a k-ω model for predicting recirculating flows. *International Journal for Numerical Methods in Fluids*, 00:1-6, 2000.

[34] L. Davidson and B. Farhanieh. CALC-BFC, a finite-volume code employing collocated variable arrangement and cartesian velocity components for computation of fluid flow and heat transfer in complex three-dimensional geometries. Chalmers University of Technology, Department of Thermo and Fluid Dynamics, 1995.

[35] P.G. Tucker and L. Davidson. Zonal $k - l$ based large eddy simulation. *Computers and Fluids*, 33:267–287, 2004.

[36] F. Hamba. A hybrid RANS/LES simulation of turbulent channel flow. *Theoretical Computational Fluid Dynamics*, 16:387–403, 2003.

[37] L. Davidson and M. Billson. Hybrid LES-RANS using synthesized turbulent fluctuations for forcing in the interface region. *Submitted, International Journal of Heat and Fluid Flows*, 2005.

[38] E. Labourasse and P. Sagaut. Reconstruction of turbulent fluctuations using a hybrid RANS/LES approach. *Journal of Computational Physics*, 182:301–336, 2002.

[39] P. Spalart, W-H. Jou, M. Strelets, and S.R. Allmaras. Comments on the feasibility of LES for wings, and on a hybrid RANS/LES approach. In *1st AFOSR International conference on DNS/LES. In advances in DNS/LES*, pages 137–147, 1997.

[40] P.G. Tucker. Differential equation-based wall distance computation for DES and RANS. *Journal of Computational Physics*, 190:229–248, 2003.

[41] F. Menter, M. Kuntz, and R. Bender. A scale-adaptive simulation model for turbulent flow predictions. In *41st Aerospace Science Meeting and Exhibit*, pages AIAA–2003–0767, 6-9 January, 2003.

[42] F. Menter and Y. Egorov. A scale-adaptive simulation model using two-equation models. In *AIAA*, pages AIAA–2005–1095, 2005.

[43] C.G. Speziale. Turbulence modeling for time-dependent RANS and VLES, a review. *AIAA Journal*, 36(2):173–184, 1998.

[44] P. Batten, U. Goldberg, and S. Chakravarthy. LNS-an approach towards embedded LES. In *40th AIAA Aerospace Sciences Meeting and Exhibit*, pages AIAA–2002–0427, 14-17 January, 2002.

[45] P. Batten, U. Goldberg, and S. Chakravarthy. Interfacing statistical turbulence closures with large-eddy simulations. *AIAA Journal*, 42(3):485–492, 2004.

[46] E. Achenbach. Distribution of local pressure and skin friction around a circular cylinder in cross-flow up to Re= $5 \cdot 10^6$. *Journal of Fluid Mechanics*, 34(4), 1968.

[47] E. Achenbach. Experiments on the flow past spheres at very high Reynolds numbers. *Journal of Fluid Mechanics*, 54(3), 1972.

[48] S.D. Stearns and R.A. David. *Signal processing algorithms in Matlab*. Prentice Hall, 1996.

A Comments on signal analysis

When solving the flow field in the time domain, the outcome will be a truncated time sequence of the variable of interest. For turbulent flows the time sequence will typically have a random character with a more or less pronounced small banded content. Unfortunately, an abrupt truncation of the Fourier series will result in a jump between the first and last value in the sampled sequence. In Fourier space, where the sequence is evaluated as an infinite series, the result will be a spectrum with an excessively high frequency content. This oscillatory effect is also known as Gibbs phenomenon. Approximating the truncated time sequence as an infinite Fourier sum is equivalent to applying a rectangular filter to the approximated truncated sequence

$$\Phi(t) = \xi(t) w_R(t) \tag{8}$$

where $w(t)$ is the window function, $\phi(t)$ is the truncated time sequence and $\Phi(t)$ is the approximated response function. Since an infinitely long time series is approximated by a truncation, it is reasonable to assume that the approximation improves with a longer time interval, T. However, the maximum amplitude of the oscillation is relatively constant regardless of the sequence length [48]. Since this oscillatory effect is the result of having excess amplitude in the high frequency components, it is desirable to reduce or taper off these high frequencies by some kind of weighted filter. This section presents some commonly used techniques for a simple test case and are further evaluated for a sequence from the simulation conducted. The signal used in this section is a pure sinus sequence defined as follows

$$\xi = A sin(2\pi \frac{k}{K}) \tag{9}$$

where the amplitude, A, is 1.0, k is the sample integer and K is the number of samples per period. Two sequences are treated in this section, a continuous signal, Fig. A, and a truncated signal, Fig. A.

For these two sequences, three filters are evaluated and defined as follows

$$w_R(t) = \begin{cases} 1, & 0 \leq t \leq T \end{cases}$$

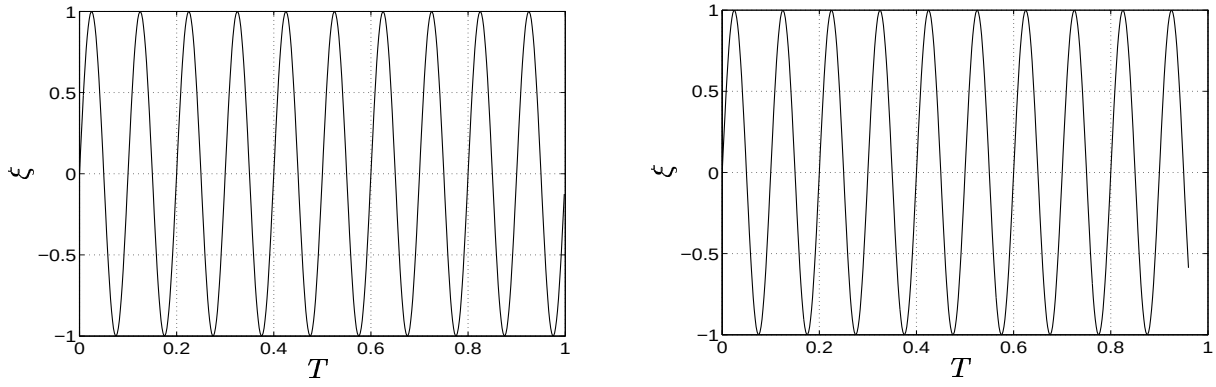

(a) Continuous sequence

(b) Truncated sequence

Figure 19: Truncated sequence

$$w_{TR}(t) = \begin{cases} \frac{1}{2}\left(1 - cos\left(\frac{t\pi}{0.1T}\right)\right), & 0 \leq t \leq 0.1T \\ 1, & 0.1T < t \leq 0.9T \\ \frac{1}{2}\left(1 - cos\left(\frac{t\pi}{0.1T}\right)\right), & 0.9T < t \leq T \end{cases}$$

$$w_H(t) = \left\{ \frac{1}{2}\left(1 - cos\left(\frac{2t\pi}{T}\right)\right), \quad 0 \leq t \leq T \right.$$

where $w_R(t)$ is the rectangular filter, $w_{TR}(t)$ is the Cosines tapered rectangular window and $w_H(t)$ is the Hanning window. These three filter functions are presented in Fig. 20.

It is clear in Fig. 20 that the three filters violate the sequence to different extents. The level can be quantified by computing the total squared window value, defined as

$$TSV = \frac{1}{N}\sum_{n=0}^{N-1} w_n^2 \tag{10}$$

The results for the three different windows are presented in Table 2. The rectangular window returns the raw sequence without any taper-

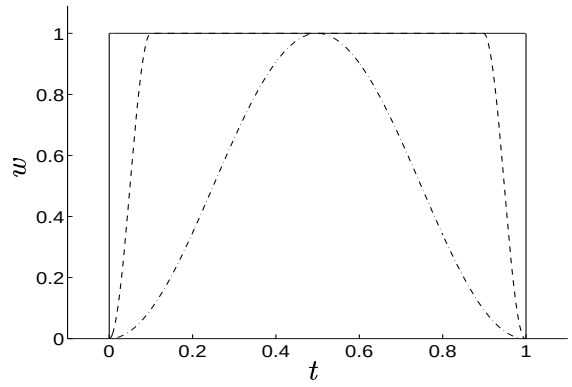

Figure 20: $(-)$ Rectangular window, $(--)$ Tapered rectangular window, $(-.)$ Hanning window

Total squared window value	
Window	TSV
Rectangular	1
Cosines-tapered	0.872
Hanning	0.374

Table 2: TSV for the different windows

ing, as discussed above. The second Cosines-tapered window leaves most of the signal unaffected and limits the amplitude reduction to the first and last 10% of the sequence. Finally, the Hanning window affects the whole sequence except the value at mid-range, resulting in a low TSV value. Another technique for evaluating a truncated sequence in the frequency plane is to compute the power spectrum from the autocorrelation of the function. The autocorrelation is defined as

$$r_{xx}(\tau) = \sum_{T} x(t)x(t+\tau)dt \tag{11}$$

where τ is the time separation. The power spectrum can then be com-

puted as

$$R_{xx}(f) = \sum_{\tau=-\infty}^{\infty} r_{xx}(\tau)e^{j2\pi f} \tag{12}$$

Two definitions will be made before studying the results. The main-lobe is identified as segments with maximum power normally defined between the points where the power has fallen $3dB$ and side-lobe segments will be defined as the frequency leakage.

Starting with Figs. 21(a) and 21(b) it can be seen that the fundamental frequency for the truncated sequence is tweaked to a higher frequency for all filtered signals except the results obtained from the autocorrelation. This is due to the Fourier transformation of the continuous autocorrelation function properly describing the actual signal without any damping, as is the case for the other windowed signals. The amplitude of the fundamental frequency is also more properly predicted with this technique, even though a slight reduction can be noticed. For the Hanning and cos-tapered filters, an underprediction in amplitude can be observed for the continuous signal and is maintained for the truncated sequence. The main and sidelobe characteristics are better presented in a log scale owing to the vast range of frequencies. In Figs. 21(c) and 21(d) the sound pressure level were computed in the following way

$$S(dB) = 10log_{10}\left(\frac{\hat{p}}{p_{ref}^2}\right) \tag{13}$$

where $p_{ref} = 2 \cdot 10^{-5}$ and $\hat{p}$ is the spectral content of the signal. It is now more obvious that the issues in amplitude for the Hanning and cos-tapered filter are compensated with a much lower side-lobe leakage compared to both the raw signal and the Fourier transformed autocorrelation. The difference can at first glance be deterring, but one must keep in mind that a 3 [dB] increase corresponds to approximately a doubling of the sound intensity.

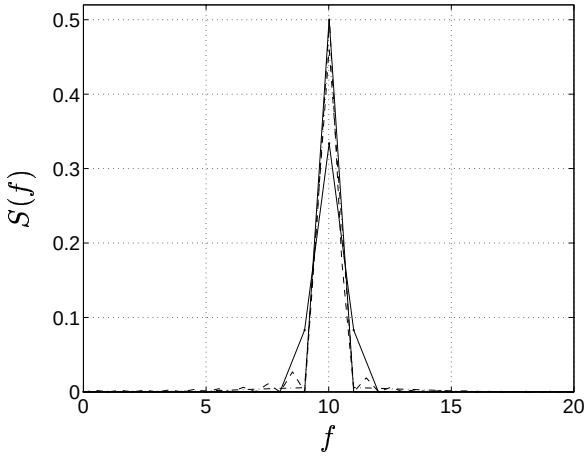

(a) Power spectrum of continuous sequence w_R (−), R_{xx} (−−), w_{RT} (−.), w_H (.)

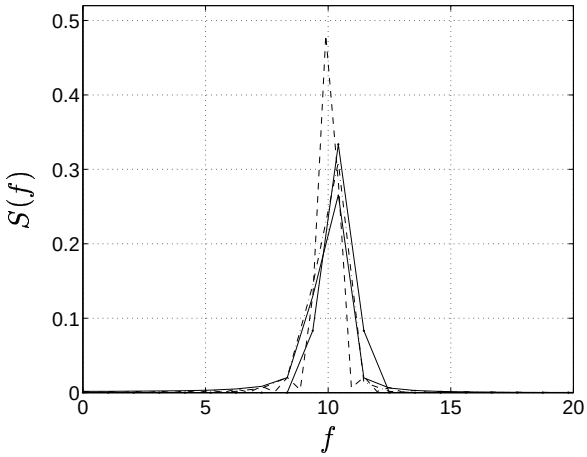

(b) Power spectrum of truncated sequence w_R (−), R_{xx} (−−), w_{RT} (−.), w_H (.)

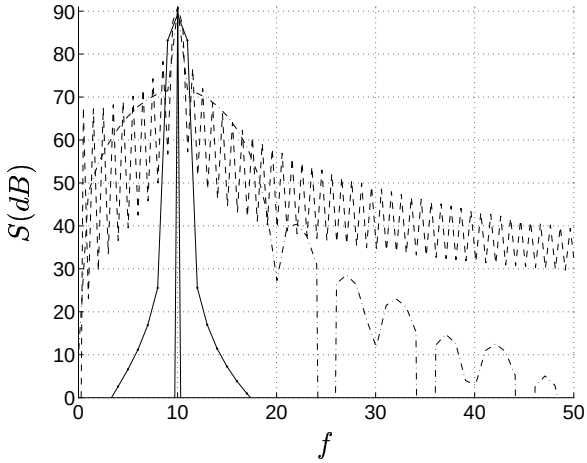

(c) SPL of continuous sequence w_R (−), R_{xx} (−−), w_{RT} (−.), w_H (.)

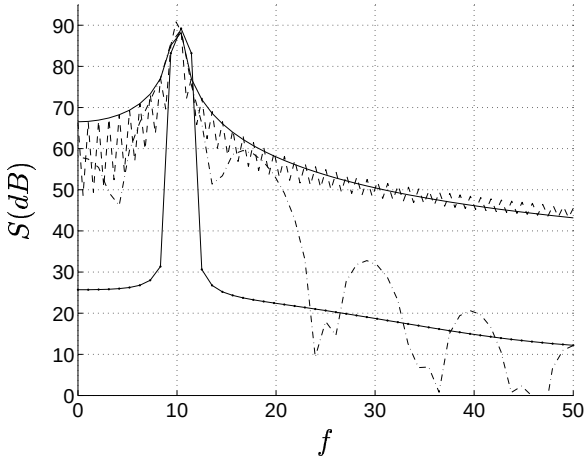

(d) SPL of truncated sequence w_R (−), R_{xx} (−−), w_{RT} (−.), w_H (.)

Figure 21: Frequency domain characteristics of a continuous sequence (left) and a truncated sequence (right)

B Microphone and Sensor positions

Positions of microphones			
Mic Id	x	y	z
M1	-1.24D	2.23D	1.2345D
M4	0.5D	1D	-2.5D
M10	2.265D	2.729D	0
M11	2.265D	2.23D	-1.2345D
M14	0.5D	8.075D	-7.1725D

Positions of instantanous pressure sensors			
Senor Id	x	y	z
S111	0.5D	0.61D	0.425D
S114	0.5D	0.61D	-0.425D
S116	-0.6D	0	0
S119	1D	0	0
S121	1.4945D	0	-0.6045D
S122	1.992D	0	-0.657D
S123	2.489D	0	-0.709D

Positions of mean pressure sensors over mirror			
Sensor Id	x	y	z
S1	0.468D	0.3335D	-0.499D
S2	0.468D	0.6665D	-0.499D
S3	0.468D	0.8335D	-0.499D
S4	0.468D	1D	-0.499D
S5	0.468D	1.129D	-0.482D
S6	0.468D	1.2495D	-0.432D
S7	0.468D	1.432D	-0.2495D
S8	0.468D	1.482D	-0.129D
S9	0.468D	1.499D	0
S10	0.3705D	1.483D	0
S11	0.25D0	1.433D	0
S12	0.1465D	1.3535D	0
S13	0.067D	1.25D	0
S14	0.017D	1.1295D	0
S15	0	1D	0
S16	0	0.833D	0
S17	0	0.6665D	0
S18	0	0.5D	0
S19	0	0.3335D	0
S20	0	0.1665D	0
S21	0.017D	0.6665D	-0.1295D
S22	0.067D	0.6665D	-0.25D
S23	0.1465D	0.6665D	-0.3535D
S24	0.25D	0.6665D	-0.433D
S25	0.3705D	0.6665D	-0.483D
S26	0.5D	0.75D	0.425D
S27	0.5D	1.4215D	-0.0555D
S28	0.5D	1.337D	-0.2585D
S29	0.5D	1.0555D	-0.4215D
S30	0.5D	0.75D	-0.425D
S31	0.5D	0.25D	-0.425D
S32	0.5D	0.25D	0
S33	0.5D	1D	0
S34	0.5D	1.25D	0